Bioorganic & Medicinal Chemistry 16 (2008) 9359–9368

Contents lists available at ScienceDirect

Bioorganic & Medicinal Chemistry

journal homepage: www.elsevier.com/locate/bmc

# Novel insights into GPCR—Peptide interactions: Mutations in extracellular loop 1, ligand backbone methylations and molecular modeling of neurotensin receptor 1

Steffen Härterich, Susanne Koschatzky, Jürgen Einsiedel, Peter Gmeiner *

*Department of Chemistry and Pharmacy, Emil Fischer Center, Friedrich Alexander University, Schuhstrasse 19, D-91056 Erlangen, Germany*

ARTICLE INFO

*Article history:*
Received 8 May 2008
Accepted 22 August 2008
Available online 27 August 2008

Dedicated to Professor H.-D. Stachel on the occasion of his 80th birthday.

*Keywords:*
Neurotensin receptor
Neuropeptide receptor interactions
Molecular modeling
Extracellular loop 1
Radioligand binding
Site-directed mutagenesis
Peptide backbone modifications

ABSTRACT

Investigating prototypical interactions between NT(8–13) and the human neurotensin receptor 1 (hNTR1), we created a receptor–ligand model that was validated by site-directed mutagenesis and structure–activity relationship studies. Stabilization of the extracellular loop 1 (EL1) by π-stacking clusters proved to be important for agonist binding when substitution of six conserved amino acids by alanine resulted in an agonist specific loss of maximal binding capacity. In agreement with our modeling studies, EL1 seems to adopt a clamp-type border area controlling the shape of the binding site crevice. Employing chemically manipulated peptide analogs as molecular probes, the impact of backbone modifications on receptor–ligand interaction, especially the influence on ligand conformation, was examined in binding studies and explained by in silico analysis.



## 1. Introduction

Neurotensin (NT) is a neuropeptide that is largely distributed in the central nervous system and some regions of the periphery. When administered into the CNS, neurotensin appears to inhibit dopamine function and produce antipsychotic activity.[1] These effects are associated with the G protein-coupled neurotensin receptor 1 (NTR1).[2] As a consequence, metabolically stable NTR1 agonists that are able to cross the blood–brain barrier may have great potential for the treatment of schizophrenia.[1,3,4] Structure–activity relationship (SAR) studies including a gradual truncation of the peptide sequence and a D-amino acid scan identified the C-terminal hexapeptide NT(8–13) (H-Arg$^{8}$-Arg$^{9}$-Pro$^{10}$-Tyr$^{11}$-Ile$^{12}$-Leu$^{13}$) as the necessary and sufficient portion for both binding affinity and ligand efficacy.[5] These findings could be corroborated when we showed that formal shuffling of the amino acids 2–3, 4–5, and 6–7 did not indicate any site-specific binding for these residues (for detailed information, see Table S2 in Supplementary material). Recently, the conformation of NT(8–13) bound to NTR1 was determined by solid state NMR spectroscopy.[6] Taking advantage of these results, lactam-bridged NT(8–13) mimetics constraining the backbone dihedral angle of Pro10 were developed.[7–9] Previous binding site models of NTR1 offered valuable insights into key interactions and basic structural elements for species specifity.[10,11] To further elucidate structural and functional properties of peptidergic GPCRs, in general and to advance a recently published pharmacophore model for NTR1 agonists,[12] we attempted to combine structure–activity relationship studies, molecular modeling and site-directed mutagenesis. Exploiting NTR1 as a prototypical peptide GPCR, our investigations especially aimed to identify conserved structural and functional motifs within the extracellular loop region and thus, influence the design of new ligands for NTR1.

## 2. Results

### 2.1. Protein sequence alignment

The crystal structure of rhodopsin is widely used as a template in GPCR homology modeling and at the time this model was cre-

*Abbreviations:* TM, transmembrane helix; EL, extracellular loop; SCR, structurally conserved region; GPCR, G protein-coupled receptor; NT, neurotensin; NT(8–13), peptide containing residues 8–13 of neurotensin; hNTR1, human neurotensin receptor 1; RMSD, root mean square deviation; MD, molecular dynamics; DPPC, 1,2-dipalmitoyl-sn-glycero-3-phosphocholine; AUC, area under the curve; SAR, structure–activity relationship.

* Corresponding author. Tel.: +49 9131 8529383; fax: +49 9131 8522585.
*E-mail address:* gmeiner@pharmazie.uni-erlangen.de (P. Gmeiner).

0968-0896/$ - see front matter © 2008 Elsevier Ltd. All rights reserved.
doi:10.1016/j.bmc.2008.08.051

ated this was the only GPCR whose crystal structure had been solved.[13–15] Our homology modeling concept was based on a protein sequence alignment which helps to identify structurally conserved regions (SCRs) present in both bovine rhodopsin and the human neurotensin receptor 1 (hNTR1). Rhodopsin and hNTR1 share only 24% sequence identity and 56% similarity within the transmembrane helix (TM) bundle. Because of the low overall identity, the alignment process was improved by the addition of 409 sequences which share the same conserved patterns, that is, other family A GPCRs.[16]

### 2.2. Membrane environment

A membrane patch, consisting of 180 1,2-dipalmitoyl-*sn*-glycero-3-phosphocholine (DPPC) lipids, was equilibrated over 3 ns of MD simulation. As a validation criterion for our membrane model, we monitored the order parameter $S_{CD}$. During the later stages of the equilibration, $S_{CD}$ closely approached experimental values[17] showing an area per lipid head group of 0.66 $nm^2$ (experiment: 0.62 $nm^2$) [18] and the expected distribution of water and lipid head group densities. After integration of the receptor into the equilibrated membrane patch,[19] polar residues pointing outwards at the extra- and intracellular side of the TMs were used as additional markers for solvent exposition and helped to validate the position of the receptor model within the membrane.

### 2.3. Molecular dynamics simulation

During the ensuing MD simulation, the general structure of the TM bundle remained stable. As expected, the highest conformational flexibility could be observed in the loop regions, especially in intracellular loop 3, which, however, refolded and finally adopted a stable conformation. After 5500 ps of simulation time, a stable root mean square deviation (RMSD) of the SCRs of about 0.23 nm (Fig. 1) and stable potential and kinetic energies indicated that the receptor model had reached equilibrium state. Extracellular loop 3 (EL3), which is expected to be of special importance for ligand binding[2] gave an acceptable RMSD value of 0.32 nm (Fig. 1). Structures in the ensuing timeframe (5500–6500 ps) were employed for the calculation of the averaged receptor model used for docking.

During the timeframe used for the averaged model, amino acids Asp138 and Arg142 formed ionic interactions with the polar head groups of two phospholipid molecules in the vicinity of the extracellular end of TM3 which were indicated by mean distances between 0.44 and 0.48 nm. In accordance with recent observations

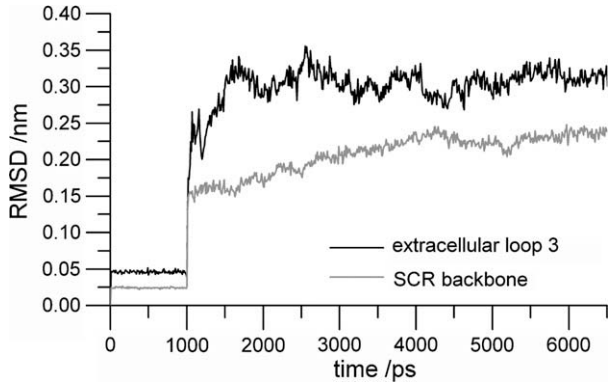


**Figure 1.** RMSD of the receptor model during equilibration. RMSD of the backbone of EL3 (black) and of the backbone of the SCRs (gray) is shown as a function of MD simulation time. The timeframe between 5500 and 6500 ps, showing stable values, is used for the generation of the equilibrated receptor model applied for docking.

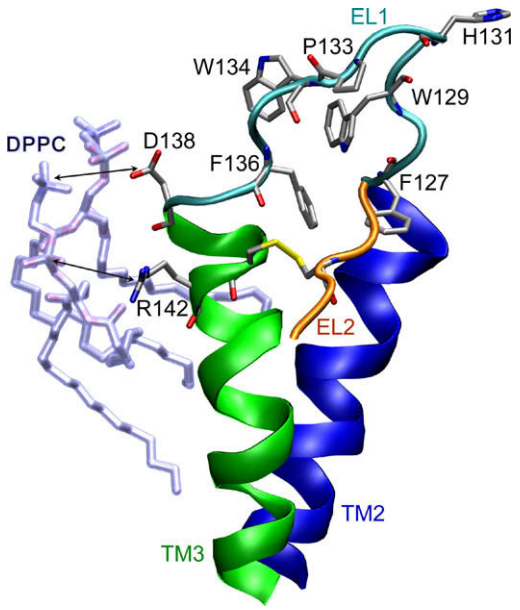


**Figure 2.** Membrane snorkeling. Representation of the final docked structure, showing the orientation of Asp138 and Arg142 towards the hydrophilic head group of two DPPC molecules as indicated by two arrows. Parts of TM2, TM3 and EL1 are represented as colored ribbons (TM2 in blue, TM3 in green, and EL1 in cyan). The aromatic cluster formed by the conserved amino acids that were mutated in this study is also shown.

described by Hawtin et al. for the V1a vasopressin receptor,[20] these residues fulfill the function of a molecular anchor that fixes the upper region of TM3 to the membrane (Fig. 2).

### 2.4. Docking

To guide and validate the docking procedure, interacting key residues derived from mutagenesis studies and solid state NMR experiments were identified,[10,21] receiving distance restraints between ligand and receptor side chains. Data from further solid state NMR experiments guided dihedral angle restraints and the starting conformation of NT(8–13).[6] A docking position between the extracellular ends of TM6, TM7, and EL2 was defined for the C-terminal carboxyl function, the adjacent $C_\alpha$ and the β-positioned $CH_2$ moiety at a place where the carboxyl group was able to interact with Arg322. In the first ensemble of structures generated with the MODELLER program package,[22] Met207 at the junction between TM4 and EL2 was too far away from the ligand binding site to form the presumed hydrophobic interactions with Ile12 and Leu13 of NT(8–13). Secondary structure consensus prediction of EL2, which was modeled in analogy to bovine rhodopsin, keeping the conserved disulfide bond between Cys141 (TM3) and Cys224 (EL2) and the hairpin structure, did not indicate a preferred folding. Therefore, we chose to remodel the region between Met203 and Asp215. A gap was introduced in the alignment file used for MODELLER, which resulted in loop structures which only had to fulfill a distance restraint between Met207 and Ile12, Leu13 of the ligand. This procedure led to an ensemble of diverse loop conformations and allowed Met207 to take part in the formation of a hydrophobic pocket for the side chain of Ile12.

For further refinement of receptor–ligand interactions, side chain atoms of the residues in EL3 were omitted in the input file. This procedure retained the backbone conformation derived from MD but removed the bias of chi angle restraints, thus resulting in higher side chain flexibility during the modeling process. In order to allow some kind of annealing process between receptor and ligand, side chain atoms of NT(8–13), except for Pro10, were also

omitted. The best model was reintegrated into the membrane environment and subjected to MD simulation. To detect favorable ensembles of ligand–receptor interactions within the resulting trajectory, two-dimensional root mean square deviation (2D-RMSD) plots were generated using the GROMACS routine *g_rms*.[23,24] RMSD was calculated on the ligand's backbone atoms and on the backbone atoms of the key residues Met207, Arg322, Phe326, Trp334, Tyr339, and Tyr342 which are supposed to take part in ligand binding.[10] The resulting plot was used to identify five homologous clusters within the trajectory, marking stable receptor–ligand interaction and stages of conformational evolution. As expected, the largest changes could be observed during the first stages of the restraintless MD simulation, finally leading to the most stable conformation found in the last cluster. Coordinate-averaged structures of each cluster were calculated. Then, RMSD values between this structure and every snapshot in the cluster were calculated in order to identify the cluster's single structure with the lowest RMSD. This timeframe was used as a representative for the cluster and for energy minimization, followed by evaluation by DrugScore$^{CSD}$,[25] indicating cluster 5 as the best docked structure. During the simulation, NT(8–13) moved away from the TM bundle towards the core of EL3. This movement still allowed an ionic interaction between Arg322 at the ligand's C-terminal end and provided a close contact of the Tyr11 side chain with an aromatic pocket at the receptor formed by Trp374, Tyr339, Tyr342, and His218 (Fig. 3A). The N-terminal end of NT(8–13) moved upwards into a position near the outer regions of EL3, allowing Arg9 to interact with Trp334. Before the last cluster was generated, the guanidinium group of Arg8 settled above Trp334, where it interacted with the backbone oxygen of Gln333 and the side chain of Thr335 (Fig. 3A and B). Additionally, a large cavity was observed around the ligand's C-terminal end which was only partly filled by the Leu13 side chain.

Analysis of the dihedral angles of NT(8–13) and subsequent comparison with the backbone conformation obtained from NMR investigations[6] showed agreement for psi 9, 11, and 12 and for phi 12 (Table 1). Deviations were found for Arg8 psi and Arg9 phi angles. The calculated phi angle of Pro10 was in a narrow range between −60° to −80°, being more likely for a proline residue than the proposed −147° of the NMR based structure.[6,26] Deviations observed for psi 10 and phi 11 antagonized each other. The fluctuation of these angles was especially pronounced between cluster 3 and cluster 5, changing from 137° and −143° in cluster 3 to 86° and −90° in cluster 5 for psi 10 and phi 11, respectively (Table 1).

Comparison of the recently solved crystal structure of a beta adrenoceptor (PDB code 2RH1) with our hNTR1 model indicates an RMSD value of 0.33 nm for the SCR backbone.[27] The value between our model and rhodopsin is 0.27 nm. The overall shape of the model shows a larger kink in TM1 and a lesser kink in TM5 as compared to rhodopsin and thus, showing similarity to the beta adrenoceptor.

### 2.5. Binding studies

Extracellular loop 1 (EL1) contains a high number of amino acids conserved among NTR1 and NTR2 species variants.[2] Nevertheless, in the described model, we could not detect any direct interactions between NT(8–13) and EL1, although it is positioned directly opposite of the binding site at EL3. To assess the importance of EL1 and prove our model's explanatory power, we constructed single point mutations of the most conserved aromatic amino acids and one proline in EL1. Interestingly, mutants F127A, H131A, P133A, and F136A showed no change in affinity for NT(8–13) and only a minor decrease in affinity for the antagonist SR 48692 when compared to the wild-type receptor. However, the amount of available binding sites was strongly reduced for the agonist NT(8–13) (Fig. 4). On the other hand, $B_{max}$ values for the antagonist SR 48692 remained unchanged, showing that the reduction in agonist binding sites was due to the mutation and not caused by reduced receptor expression. The binding site of SR 48692 is supposed to be situated between the TMs, partly overlapping with the binding site of NT.[2] Therefore, it should be less affected by mutations in the extracellular loop region and reflect correct folding and correct arrangement of the TM bundle. Comparison of the ratio between $B_{max}$ values of NT(8–13) and SR 48692 for the wild-type and mutant receptors showed that the

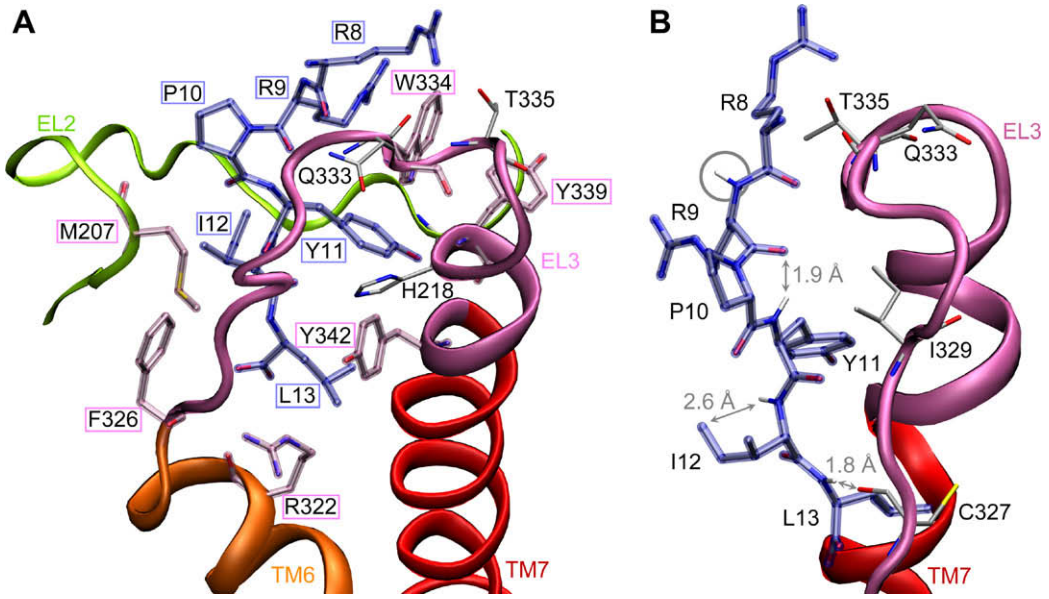


**Figure 3.** Best docked structure. Representation of cluster 5 with NT(8–13) docked into hNTR1. Not all residues are displayed. Residues of the ligand and of the presumed binding site are coated in blue and pink, respectively. (A) Binding site at EL3, showing the aromatic pocket (H218, Trp334, Tyr339, and Tyr342) for Tyr11, the ionic interaction of the ligand's C-terminal end with the side chain of Arg322 and the interaction of Arg8 with Gln333 and Thr335 above EL3. (B) Putting special emphasis on ligand backbone interaction. $N_\alpha$–H of Arg9 is oriented towards the solvent. Ile329 and the backbone oxygen of Arg9 are in the vicinity of $N_\alpha$–H of Tyr11. The side chain of Ile12 is next to its own $N_\alpha$–H position. $N_\alpha$–H of Leu13 forms an H-bond with the backbone oxygen of Cys327.

**Table 1**
Backbone dihedral angles of NT(8–13) observed in the clusters

| Angle | Lit.[a] | Cluster 1 | Cluster 2 | Cluster 3 | Cluster 4 | Cluster 5 |
|---|---|---|---|---|---|---|
| R8 psi | −34 ± 15 | 120 ± 16 | 124 ± 16 | 122 ± 14 | 123 ± 19 | 110 ± 15 |
| R9 phi | −134 ± 31 | −131 ± 16 | −131 ± 16 | −130 ± 16 | −128 ± 21 | 53 ± 17 |
| R9 psi | 136 ± 25 | 103 ± 12 | 112 ± 9.2 | 99 ± 10 | 117 ± 13 | 113 ± 10 |
| P10 phi | −147 ± 16 | −72 ± 11 | −69 ± 8.8 | −68 ± 11 | −70 ± 10 | −73 ± 8.8 |
| P10 psi | 146 ± 15 | 119 ± 31 | 111 ± 23 | 137 ± 25 | 101 ± 26 | 86 ± 18 |
| Y11 phi | −121 ± 22 | −111 ± 31 | −109 ± 24 | −143 ± 22 | −104 ± 27 | −90 ± 21 |
| Y11 psi | 131 ± 19 | 134 ± 14 | 132 ± 13 | 138 ± 15 | 147 ± 12 | 139 ± 15 |
| I12 phi | −114 ± 8 | −115 ± 15 | −109 ± 15 | −119 ± 15 | −126 ± 13 | −125 ± 15 |
| I12 psi | 134 ± 24 | 150 ± 11 | 151 ± 12 | 156 ± 14 | 157 ± 14 | 155 ± 14 |
| L13 phi | −104 ± 16 | −129 ± 11 | −139 ± 15 | −145 ± 14 | −144 ± 14 | −142 ± 14 |

Data represents mean values and standard deviation as observed for NT(8–13) in the docked MD simulation.
[a] See Luca et al. [6]

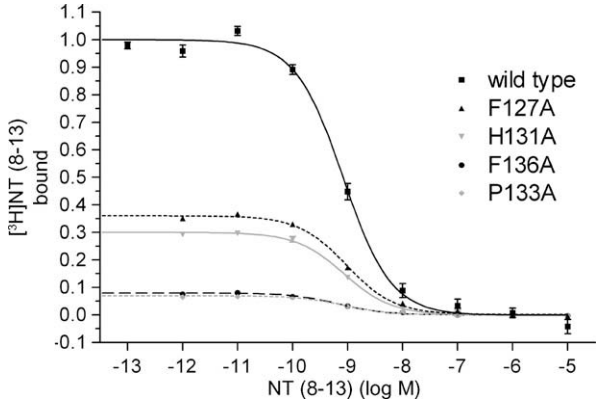


**Figure 4.** Competition binding curves. Graph showing the data obtained in homologous competition binding assays with [$^3$H]NT(8–13) at receptors mutated at EL1. Values from the competition binding assays were normalized for each receptor mutant and multiplied with the corresponding $B_{max}$ SR 48692/NT(8–13) ratio, showing the reduction in specific receptor binding of NT(8–13).

amount of agonist binding sites was reduced to less than 10% for P133A and F136A. No specific binding could be detected for NT(8–13) at the W129A and W134A mutants. On the other hand, ligand affinity of SR 48692 remained almost unchanged when compared to the wild-type (Table 2).

To break down the binding energy to specific contacts and, thus, the influence of backbone-induced H-bonds and conformational restraints, a microwave assisted solid-phase peptide synthesis protocol was applied to yield the backbone methylated NT(8–13) analogs [*N*-Me-Arg$^9$]NT(8–13) (**1**), [*N*-Me-Tyr$^{11}$]NT(8–13) (**2**),[7] [*N*-Me-Ile$^{12}$]NT(8–13) (**3**), and [*N*-Me-Leu$^{13}$]NT(8–13) (**4**). Receptor binding studies of the NT(8–13) surrogate **1** showed that substitution at Arg9 did not significantly influence ligand affinity ($K_i$ 0.51 nM). This indicates that the disposition might be at a sterically less demanding entrance of the binding pocket. On the other hand, exchange of Ile12 and Leu13 led to a more than 200-fold reduction of binding (Table 3), indicating a loss of backbone interaction or conformational torsion. Even more, introduction of *N*-Me-Tyr$^{11}$ resulted in only poor affinity to the active conformation of hNTR1 labeled with [$^3$H]NT(8–13) and a $K_i$ that was almost 10,000-fold below the $K_d$ value (Table 3). Our ligand–receptor model indicated that this difference is the effect of intramolecular clashes of the introduced *N*-methyl substituent with the carbonyl oxygen of the *N*-acylproline unit (Fig. 3B). Alternatively, repulsive receptor–ligand interactions with Tyr328, Ile329, and Ser330 could be responsible for the poor radioligand displacement. Especially the side chain of Ile329 was in close vicinity of Tyr11-$N_\alpha$ and seemed to take part in receptor–ligand interaction (Fig. 3B). Thus, we constructed the I329G single and YIS328-330AAA triple mutants. However, the affinity of both NT(8–13) and the congener **2** was unaffected by these mutations (Table 3). The binding affinity of the adamantane amino acid substituted derivative [Aac$^{13}$]NT(8–13) (see experimental), was comparable to NT.

**Table 3**
Effect of backbone methylation on ligand affinity and efficacy

| Compound | [$^3$H]NT(8–13) displacement (±SEM) | Rel. $Ca^{2+}$ signal (±SEM) |
|---|---|---|
| NT | 2.1 nM (±12%) | 100% (±16%) |
| NT(8–13) | 0.63 nM (±11%) | 385% (±24%) |
| [N-Me-Arg$^9$]NT(8–13) | 0.51 nM (±5.7%) | 362% (±17%) |
| [N-Me-Tyr$^{11}$]NT(8–13) | 5.1 μM (±21%) | −154% (±52%) |
| [N-Me-Ile$^{12}$]NT(8–13) | 0.16 μM (±19%) | 96% (±8%) |
| [N-Me-Leu$^{13}$]NT(8–13) | 0.19 μM (±17%) | 238% (±9%) |
| [Aac$^{13}$]NT(8–13) | 2.4 nM (±8.7%) | 180% (±11%) |
| Receptor | $K_d$ NT(8–13) | $K_i$ compound **2** |
| Wild-type | 0.63 nM (±11%) | 5.1 μM (±21%) |
| I329G | 0.47nM (±23%) | 4.1 μM (±19%) |
| YIS328-330AAA | 0.80 nM (±36%) | 7.1 μM (±39%) |

Data obtained from competition binding assays with [$^3$H]NT(8–13) (2–8 experiments in triplicate). Relative calcium signal refers to calcium levels observed at 100 nM relative to NT.

**Table 2**
Radioligand binding studies at the EL1 mutants

| Receptor | $K_d$ NT(8–13) | $B_{max}$ (pmol/mg) | $K_d$ SR 48692 | $B_{max}$ (pmol/mg) | $B_{max}$ SR 48692/NT(8–13) (%) |
|---|---|---|---|---|---|
| Wild-type | 0.63 nM (0.49–0.80) | 11 | 8.9 nM (7.5–11) | 15 | 100 |
| F127A | 0.74 nM (0.60–0.94) | 4.8 | 19 nM (12–29) | 18 | 36 |
| W129A | Not detectable | — | 27 nM (19–38) | 9.4 | — |
| H131A | 0.64 nM (0.51–0.84) | 3.5 | 8.4 nM (6.9–10) | 16 | 30 |
| P133A | 0.64 nM (0.39–1.1) | 0.47 | 9.2 nM (7.1–12) | 9.3 | 7 |
| W134A | Not detectable | — | 23 nM (12–44) | 10 | — |
| F136A | 0.46 nM (0.36–0.64) | 0.71 | 33 nM (17–62) | 10 | 9 |

Data are derived from normalized curves of 4–6 experiments done in triplicate (values in brackets are 95% confidence intervals). $B_{max}$ ratio percentages are calculated relative to the wild-type receptor ratio.
Data obtained from homologous competition binding assays with [$^3$H]NT(8–13) and [$^3$H]SR 48692, respectively.

### 2.6. Ligand potency

In order to evaluate the effect of backbone methylation on $G_q$ transactivation, the *N*-methyl substituted peptide analogs **1**–**4** were tested for their ability to increase the intracellular calcium concentration. Comparison of calcium release at concentrations of 100 nM indicated, that **1** was almost as effective as NT(8–13) whereas **3** and **4** showed reduced activation properties (Table 3). These results were in agreement with data from receptor binding studies. [*N*-Me-Tyr$^{11}$]NT(8–13), however, reduced the calcium signal to −154% which is comparable to neurotensin when the absolute values are compared. To further investigate this effect, the experiments were performed at different concentrations revealing a dose-dependent inverse agonist effect of [*N*-Me-Tyr$^{11}$]NT(8–13) (**2**) (Fig. 5). This effect is specifically mediated by the hNTR1 as calcium levels in untransfected HEK cells did not differ from control upon administration of **2**.

### 2.7. Conformational energy calculations

To examine the effect of backbone methylation on the conformation of NT(8–13), force field based energy maps were created, based on a capped alanine tripeptide as truncated model peptide. For Arg9, Tyr11, Ile12, and Leu13 both maps, representing methylated and non-methylated model peptides, had low energy phi and psi angles corresponding to those found in the trajectory. Backbone dihedral angles of Pro10 next to the methylated residue regarding [*N*-Me-Tyr$^{11}$]NT(8–13) (**2**), were found in a region which partly showed an increase in conformational energy. Because of proline being a particular amino acid known to differ in its conformation from most other amino acids,[26] we also calculated conformational energy plots for N-Ac-Pro-Xxx-Ala-NMe where Xxx = Tyr and (*N*Me)Tyr. As expected, the resulting maps showed additionally confined allowed regions, but gave similar results for the observed angles. The highly correlated changes between psi of Pro10 and phi of Tyr11, observed in the trajectory, inspired us to also create conformational energy maps for the combination of these two angles, including the conformation observed in cluster 3. The results indicated that the angles of cluster 5 were at an energetically more favorable region (−1.1 kcal mol$^{-1}$) than those of cluster 3 (+1.03 kcal mol$^{-1}$) (Fig. 6). Methylation at tyrosine reversed the situation. Now the conformation observed in cluster 3 was at the rim of the energetically most favorable region (7.85 kcal mol$^{-1}$) and the conformation of cluster 5 was less favorable (12.7 kcal mol$^{-1}$).

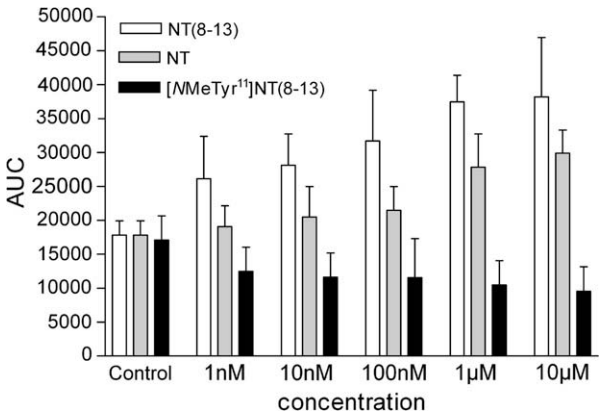


**Figure 5.** Concentration dependent calcium release. AUC of calcium fluorescence signals induced by hNTR1 activation at different concentrations of NT(8–13), NT and [N-Me-Tyr$^{11}$]NT(8–13). Control values were derived by the addition of pure buffer.

## 3. Discussion

The neurotensin receptor NTR1 is a prototypical peptidergic GPCR that plays an important role in the discovery of antipsychotic drugs. Aiming to better understand the overall shape and plasticity of the binding site crevice and to identify crucial interactions, this study benefits from a tight interplay of site-directed mutagenesis, in silico investigations and SAR studies.[12]

To make sure that the binding site of NT(8–13) is not placed within the TM bundle, like in aminergic GPCRs or opioid receptors, we created a preliminary model based on the μ opioid receptor model published by Mosberg and co-workers[28] Docking of NT(8–13) into this structure according to opioid ligands revealed that the central part of the binding pocket was lined by Arg148, Asp149, Tyr153, Tyr319, Phe35, and Tyr354. These residues have already been examined by mutagenesis studies and no direct influence on NT binding could be detected.[29] For a great number of peptidergic GPCRs, ligand binding sites are suggested to be located mainly at the extracellular ends of TM6, TM7 and the connecting EL3, which is likely to be exposed to solvent.[30] Since vacuum MD simulations can lead to severe distortions of loop structures,[31]

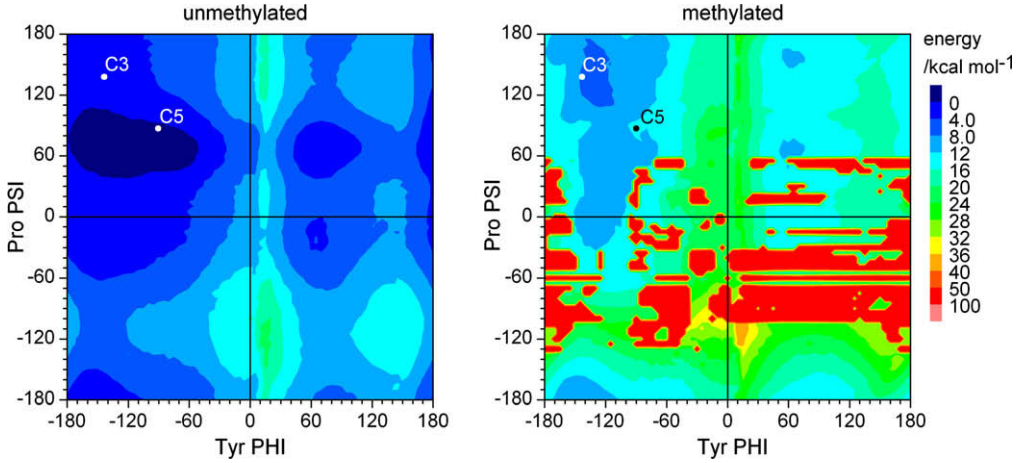


**Figure 6.** Conformational energy maps. Data obtained by GRIDSEARCH, sampling backbone phi and psi angles of N-Ac-Pro-Xxx-Ala-NMe where Xxx = Tyr and (NMe)Tyr. Angles found in clusters 3 and 5 are indicated in the plots. The combination of proline-psi and tyrosine-phi angles is depicted, showing an increase in conformational energy upon methylation.

we chose an explicit water/membrane environment for the equilibration of our rhodopsin-based homology model, which adopted a stable conformation after moderate MD simulation time.

Instead of creating a single heuristic best model, we took advantage of an efficient docking procedure, building and scoring an ensemble of different models.[32] Since we expected the structurally nonconserved extracellular loop 3 to form a significant part of the binding site of NTR1, we chose to dock our ligand into a model, in which the carefully constructed EL3 had already been intensely equilibrated. MD simulation of the ligand–receptor complex allowed ligand and receptor to adapt to each other and form energetically favorable interactions, finally leading to cluster 5 with the best DrugScore result and lowest RMSD of the binding site. The obvious improvement during the first quarter of the MD simulation was caused by the described movement of NT(8–13) towards the aromatic pocket at EL3. Peptide backbone dihedral angles agreed with experimentally derived values for psi 9, 11, and 12 and for phi 12. Deviations, observed at psi 8 and phi 9, were probably due to the solvent exposed position of Arg8. High flexibility existed in this residue's side chain until it finally settled at the described site above EL3. The correlated shifts in psi 10 and phi 11 were due to flexibility in the backbone orientation while the side chains of the two residues showed only minor fluctuations.

Besides the above discussed primary binding site that proved to form a tunnel between extracellular loop 3, TM6 and TM7, extracellular loop 1 was expected to build a crucial border area. Interestingly, a DXXCR motif at the interface between TM3 and EL1 is conserved among peptidergic GPCRs and it was shown for the $V_{1A}$ vasopressin receptor that this motif is important for receptor activation.[20] NTR1 mutants R142G and D138A were reported earlier to lead to a complete loss of ligand binding but no explanation could be provided.[2] As observed in our MD simulation, these two residues 'snorkeled' in the membrane/water interface region,[33] thereby anchoring the position of TM3 at the membrane. Mutagenesis of the EL1 residues revealed a reduction of $B_{max}$ values in combination with no change in binding affinity of the agonist [$^3$H]NT(8–13). This data points to a loss of high affinity binding sites which are needed for receptor activation. A comparable impact was observed at some residues in EL3 which are not involved in ligand binding but receptor activation.[34] Furthermore, at the C5a receptor the conserved WXFG motif at the C-terminal end of EL1, which is also present in the hNTR1, was reported to be important for receptor activation.[35] Our homology model predicted aromatic π-stacking between Phe127, Phe136, Trp129, and Trp134. This results in a rigid EL1, forming a kind of clamp, which keeps TM3 and TM2 together. In combination with the membrane anchoring observed in our MD simulation, EL1 seems to stabilize the extracellular regions of TM2, TM3 and parts of EL2 which is connected to TM3 by a disulfide bond (Fig. 7). Perturbation of the π−π interactions in this region by means of site-directed mutagenesis obviously interferes with receptor activation and strongly reduces ligand binding.

According to our receptor model, the binding site is primarily forming a tunnel between extracellular loop 3, TM6 and TM7 harboring major parts of the residues 11, 12, and 13 whereas residues 8–10 are located at the outer surface of the loop. The cavity, which is only partly filled by Leu13, could easily accommodate a sterically highly demanding adamantane residue of the respective unnatural amino acid (Fig. 8). This observation could be verified by chemical synthesis and subsequent ligand binding experiments revealing an affinity of [Aac$^{13}$]NT(8–13) that is comparable to neurotensin ($K_i$ = 2.4 nM) (Table 3). Backbone N-methylations were chosen as a further instrument to characterize the shape of the binding pocket and the bioactive conformation of NT(8–13). Thus, methylation of $N_\alpha$ at Arg9 leads to the peptide analog [*N*-Me-Arg$^9$]NT(8–13) that showed binding properties similar to NT(8–13) which was in

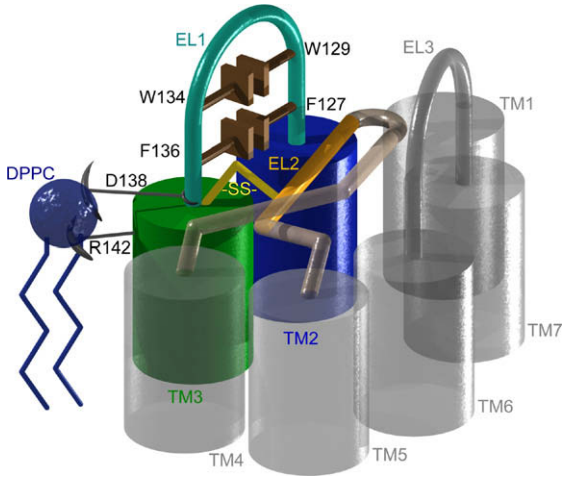


**Figure 7.** Functional role of EL1. Representation of the region around EL1 as an abstract model showing the presumed function. Asp138 and Arg142 anchor TM3 to the membrane, aromatic residues in EL1 form a rigid π-stacking cluster and the disulfide bond connects TM3 and EL2.

agreement with the model, revealing that the amide function was outward directed, lacking attractive interactions with the receptor protein. On the other hand, our model indicated a crucial H-bond between the carbonyl oxygen of Cys327 and $N_\alpha$ of Leu13 (Fig. 3B), explaining the moderate loss in affinity for [*N*-Me-Leu$^{13}$]NT(8–13) ($K_i$ = 0.19 μM). The decrease in affinity observed for [*N*-Me-Ile$^{12}$]NT(8–13) is obviously due to intramolecular steric interactions with the $CH_2CH_3$ group of the side chain (Fig. 3B). Supporting evidence is found in the literature when it was shown that exchange of the NH function by a $CH_2$ group did not alter binding affinity.[36] Special susceptibility was expected from backbone N-methylation at the Tyr11 position. We could not detect a hydrogen bond that could be lost and the triple mutant YIS328-330AAA indicated that additional space did not improve binding affinity of [*N*-Me-Tyr$^{11}$]NT(8–13). However, intramolecular clashes were detected between the *N*-methyl function and the carbonyl oxygen of Arg9. Thus, we could deduce that [*N*-Me-Tyr$^{11}$]NT(8–13) was unable to adopt a secondary structure similar to the bioactive conformation of NT(8–13) evolved from the molecular dynamics simulation. In fact, an almost 10,000-fold reduction of [$^3$H]NT(8–13) displacement was observed for [*N*-Me-Tyr$^{11}$]NT(8–13).

Comparison of the conformational energies of backbone phi/psi angles shows that methylation has little effect in regard to Arg9, Leu13, and Ile12. Methylation at Tyr11, however, considerably influences psi of Pro10 and phi of Tyr11. After methylation, the conformation observed in cluster 5 of our molecular dynamics simulation is energetically less favored. On the other hand, the intermediately generated cluster 3 of our trajectory seemed to represent a structural family that could be in good agreement with the conformational requirements for [*N*-Me-Tyr$^{11}$]NT(8–13) (**2**). Since cluster 3 is energetically less favored than cluster 5, the conformational restraint inflicted by N-methylation in position 11 might hinder the induced fit of the ligand and prevent agonist binding as well as activation. This is in agreement with data from our functional calcium assay, clearly revealing inverse agonist properties for the peptide analog **2**. As a functional switch, backbone conformation at the Pro10/Tyr11 region might be of fundamental importance for receptor activation when methylation at this position induces a change in the preferred binding mode. This would explain why the compound is a strong inverse agonist at nanomolar concentrations but shows only micromolar affinity when competing with the agonist NT(8–13).

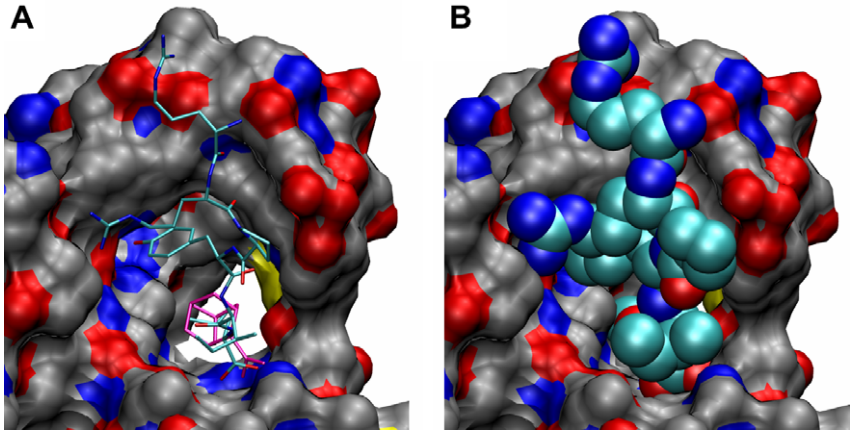


**Figure 8.** Docked NT(8–13) and [Aac$^{13}$]NT(8–13). The receptor is represented as solvent accessible surface. (A) NT(8–13) is shown in cyan, the sterically demanding adamantyl substituted Leu13 is shown in pink within the binding site tunnel. (B) NT(8–13) is shown as CPK representation within the binding site.

## 4. Conclusion

The benefit of GPCR homology modeling based on the crystal structure of bovine rhodopsin remains controversial.[14,37] In addition, we had to omit the long N-terminal and C-terminal ends in order to prevent unwanted bias. Therefore, producing and implementing experimental results obtained from chemical synthesis and site-directed mutagenesis is essential to overcome the above mentioned limitations. Recently the crystal structure of the beta adrenoreceptor has been solved and future will tell whether models based on the adrenoceptor crystal structure will be more accurate than those based on the rhodopsin crystal.

Our model correctly predicted that EL1 does not take part in ligand binding and we were able to deduce a hypothesis for the effect of mutations in EL1, based on published results, radioligand binding studies and homology modeling. This data showed that EL1 forms an integral part in receptor function and signal transmission. Furthermore we identified [*N*-Me-Tyr$^{11}$]NT(8–13) as an inverse agonist and we derived an explanation for the dramatic loss of binding affinity of this compound when compared to backbone methylation at Arg9, Ile12, or Leu13.

NT agonists and antagonists were described as potential drugs in the treatment of schizophrenia and Parkinson's disease, respectively.[1,38] In combination with a recently published pharmacophore hypothesis based on SAR studies,[12] our results will help to guide the development of new ligands for NTR1 and facilitate a better understanding of the functionality of peptidergic GPCRs.

## 5. Experimental

### 5.1. Site-directed mutagenesis

The hNTR1 cDNA, subcloned into a pcDNA3.1(+) eukaryotic expression vector, was purchased from the UMR cDNA Resource Center. Oligonucleotidic primers were purchased from Biomers.net. Site-directed mutagenesis was performed by polymerase chain reaction (PCR) using oligodeoxynucleotides bearing the desired mutation.[39] Fidelity of PCR amplification and introduction of mutations in the receptor cDNAs was confirmed by sequencing with the ABI sequencer system (ABI Systems, Weiterstadt, Germany) at the laboratory of C.-M. Becker (Department of Biochemistry, FAU Erlangen, Germany) using appropriate oligodeoxynucleotidic primers.

### 5.2. Receptor preparation

HEK-293 cells, transiently transfected with wild-type and mutant receptor cDNA by the $CaHPO_4$ method,[40] were cultured in 150-mm Petri plates containing 20 mL of MEM alpha medium supplemented with 10% (v/v) fetal bovine serum, 100 U/mL penicillin G, 100 μg/mL streptomycin, and 2 mM L-glutamine.

HEK-293 cells were harvested 48 h after transfection. Cells were removed by aspiration of the medium, followed by a wash with phosphate buffered saline, which was discarded, resuspension in 10 mL of harvest buffer (10 mM Tris–HCl, 0.5 mM EDTA, 5.5 mM KCl, and 140 mM NaCl, pH 7.4), scraping the cells with a rubber spatula into a centrifuge tube, and collection of cells by centrifugation at 220*g* for 8 min. The cellular pellet was resuspended in 5 mL of homogenate buffer (50 mM Tris–HCl, 5 mM EDTA, 1.5 mM $CaCl_2$, 5 mM $MgCl_2$, 5 mM KCl, and 120 mM NaCl, pH 7.4) and stored at −80 °C. After thawing, the cells were diluted in homogenate buffer, homogenized using a Polytron (20,000 rpm, 5 × 5 s each in an ice bath), and spun at 50,000*g* for 15 min. The membrane pellet was resuspended in storage buffer (50 mM Tris–HCl, 1 mM EDTA, 5 mM $MgCl_2$ 0.1 mM dithiothreitol, 100 μg/mL bacitracin, and 5 μg/mL soybean trypsin inhibitor, pH 7.4), homogenized with a Potter-Elvehjem homogenizer, and stored in small aliquots at −80 °C. Protein concentration of the membrane preparation was estimated by the method of Lowry et al.[41] using bovine serum albumin as a standard.

### 5.3. Radioligand binding studies

The radioligand [$^3$H]NT(8–13) was synthesized in collaboration with Amersham/GE Healthcare UK Limited and obtained with a specific activity of 136 Ci/mmol. The neurotensin receptor binding assay followed a previously published protocol[7] and was adapted to 96-well plates, employing 0.2 nM [$^3$H]NT(8–13) or 0.8 nM [$^3$H]SR 48692 (specific activity 81 Ci/mmol; Amersham Biosciences UK Limited), respectively. Unlabeled SR 48692 was a generous gift from the Chemical Synthesis and Drug Supply Program of the National Institute of Mental Health. $K_i$ values were derived from the corresponding $EC_{50}$ data.[42]

### 5.4. Functional calcium assay

Fluorescence measurement of intracellular calcium release was carried out applying a Victor$^3$V multilabel counter (Perkin Elmer, Freiburg, Germany) with a 485/510 nm filter set, following an adapted protocol published by Lee et al.[43] and Kassack et al.[44] In

brief, HEK-293 cells were harvested 48 h after transient transfection with wild-type hNTR1 cDNA and kept at 37 °C/5% $CO_2$ for 15 min. After centrifugation, the cell pellet was washed once with calcium free Krebs-Hepes buffer (118 mM NaCl, 4.7 mM KCl, 1.2 mM $MgSO_4$, 1.2 mM $KH_2PO_4$, 4.2 mM $NaHCO_3$, 117 mM D-glucose, and 10 mM Hepes, pH 7.4) and incubated with 2 μM Fluo-4 AM (Invitrogen, Karlsruhe, Germany) and 2.5 mM probenecid (Sigma–Aldrich, Steinheim, Germany) for 1 h in the dark at 37 °C/5% $CO_2$. Cells were washed two times and split in 96-well plates with $10^5$ cells in 80 μL Krebs-Hepes buffer per well. Plates were kept at 37 °C/5% $CO_2$ for 30 min. Baseline fluorescence was measured for 48 s. The fluorescence signals of agonist stimulated alterations in intracellular calcium levels were collected at 8 s intervals for 200 s. Data were analyzed using PRISM (GraphPad Software, San Diego, CA). For quantification of ligand efficacy, the area under the curve (AUC) was calculated from the fluorescence signals of −16 s to +48 s, the test compound being added at 0 s. The average value of the fluorescence signals from 56 to 200 s was used for baseline correction.

### 5.5. Peptide synthesis

General method for the microwave assisted Fmoc deprotection/acylation procedure: the peptide synthesis was achieved by manual microwave assisted solid-phase techniques starting from the respective resin. Amino acids were incorporated as their commercially available derivatives in the following order: Fmoc-*N*-Me-Leu-OH, Fmoc-Ile-OH, or Fmoc-*N*-Me-Ile-OH, Fmoc-Tyr(*t*Bu)-OH, Fmoc-Pro-OH, Fmoc-Arg(Pbf)-OH, or Fmoc-*N*-Me-Arg(Mtr)-OH, Fmoc-Arg(Pbf)-OH. If not specified more precisely, elongation of the peptide chain was done by repetitive cycles of Fmoc deprotection applying 20% piperidine in DMF (microwave irradiation: 5 × 5 s, 100 W), followed by 5 washings with DMF and subsequent peptide coupling employing 5 equiv of the corresponding Fmoc-amino acid/PyBOP/diisopropylethylamine and 7.5 equiv HOBt, dissolved in a minimum amount of DMF (irradiation: 15 × 10 s, 50 W). In between each irradiation step, cooling of the reaction mixture to a temperature of −10 °C was achieved by sufficient agitation in an ethanol-ice bath. Coupling of the amino acid next to the N-methylated derivative was performed with BTC/2,6-lutidine in dioxan. After the last acylation step the N-terminal Fmoc-residue was deprotected, the resin was rinsed ten times with $CH_2Cl_2$ and dried in vacuo. The cleavage from the resin was performed using a mixture of TFA/phenol/$H_2O$/triisopropylsilane 88:5:5:2 for 2 h, in case of peptide **1** for 6 h. After evaporation of the solvent and precipitation in *tert*-butylmethylether, the crude peptides were purified using preparative RP-HPLC and subsequent lyophilization. Peptide purity and identity were assessed by analytical HPLC. The procedures yielded the N-methylated peptides [*N*-Me-Arg$^9$]NT(8–13) (**1**), [*N*-Me-Ile$^{12}$]NT(8–13) (**3**), [*N*-Me-Leu$^{13}$]NT(8–13) (**4**), and the NT(8–13) derivative [Aac$^{13}$]NT(8–13) **(5)** with 2-aminoadamantane-2-carboxylic acid in position 13.

#### 5.5.1. Purification of the peptides

Preparative RP-HPLC (Agilent 1100 preparative series) was performed applying the following conditions (if not noted more specifically): column: Zorbax Eclipse XDB-C8, 21.2 × 50 mm, 5 μm particles, eluent: 0.1% TFA in acetonitrile (A) and 0.1% TFA in $H_2O$ (B) applying a linear gradient starting from 5% A in 95% B, flow rate: 18 mL/min. Peptide purity and identity were assessed by analytical HPLC (Agilent 1100 preparative series, column: Zorbax Eclipse XDB-C8 analytical column, 4.6 × 150 mm, 5 μm, flow rate: 0.5 mL/min, detection wavelength: 220 nm) coupled to a Bruker Esquire 2000 mass detector equipped with an ESI-trap. System 1 (S1) if not noted more specifically: 10–55% $CH_3OH$ in $H_2O$ + 0.1% $HCO_2H$ in 18 min, System 2 (S2) if not noted more specifically: 3–40% $CH_3CN$ in $H_2O$ + 0.1% $HCO_2H$ in 26 min.

#### 5.5.2. H-Arg-*N*-Me-Arg-Pro-Tyr-Ile-Leu-OH ([*N*-Me-Arg$^9$]NT(8–13)) (1)

The synthesis was performed starting from commercially available Fmoc-Leu-Wang resin. Fmoc-*N*-Me-Arg(Mtr)-OH and Fmoc-Arg(Pbf)-OH were each coupled using a double coupling, first acylation: amino acid/HATU/DIPEA 5 equiv/5 equiv /5 equiv second acylation: BTC protocol as described for peptide **4**, both cycles under microwave irradiation. Purification: gradient: 5–22% A in 26.9 min, then isocratic elution, $t_R$: 28.7 min, ESI-MS: $[M+H]^+$; Calcd: 831.5, found: 831.5. Purity: S1: >99% ($t_R$: 12.7 min); S2: >99% ($t_R$: 14.1 min).

#### 5.5.3. H-Arg-Arg-Pro-Tyr-*N*-Me-Ile-Leu-OH ([*N*-Me-Ile$^{12}$]NT(8–13)) (3)

The synthesis was performed starting from commercially available Fmoc-Leu-Wang resin (loading 0.8 mmol/g). PyBOP-coupling of Fmoc-*N*-Me-Ile-OH was repeated 2× and the following Fmoc-Tyr-OH was coupled with BTC as described for peptide **4** (single coupling without microwave). Purification: gradient: 5–26% A in 26.9 min, $t_R$: 23.8 min, ESI-MS: $[M+H]^+$ Calcd: 831.5, found: 831.6. Purity: S1: 99% ($t_R$: 13.8 min); S2: 98% ($t_R$: 14.5 min).

#### 5.5.4. H-Arg-Arg-Pro-Tyr-Ile-*N*-Me-Leu-OH ([*N*-Me-Leu$^{13}$]NT(8–13)) (4)

Commercially available 2-chlorotritylchloride resin (loading: 1.9 mmol/g) was stirred in a solution of Fmoc-*N*-Me-Leu-OH (1 equiv)/ diisopropylethylamine (DIPEA, 4 equiv) in $CH_2Cl_2$. After 2 h the resin was washed 3× with $CH_2Cl_2$/$CH_3OH$/DIPEA (17:2:1), 3× $CH_2Cl_2$, 2× DMF, 2× $CH_2Cl_2$ and dried in vacuo. After removing the Fmoc group, Fmoc-Ile-OH (5 equiv) was activated with BTC[45] (1.67 equiv) and 2,6-lutidine (12.50 equiv) in dioxane and added to the resin, that was suspended in a solution of DIPEA (10 equiv) in dioxane.

BTC-coupling was repeated using microwave irradiation and peptide synthesis was finished according to the protocol described above. Purification: gradient: 5–30% A in 26.9 min, $t_R$: 24.2 min, ESI-MS: $[M+H]^+$; Calcd: 831.5, found: 831.6. Purity: S1: 98% ($t_R$: 15.3 min); S2: 98% ($t_R$: 16.0 min).

#### 5.5.5. H-Arg-Arg-Pro-Tyr-Ile-Aac-OH ([Aac$^{13}$]NT(8–13)) (5)

At first, Fmoc-2-aminoadamantane-2-carboxylic acid (Fmoc-Aac) was synthesized. 2-Aminoadamantyl-2-carboxylic acid hydrochloride (509 mg, 2.20 mmol) was suspended in $CH_2Cl_2$ (20 mL) and subsequently treated with DIPEA (1.13 mL, 6.60 mmol) and TMSCl (280 μL, 2.20 mmol). The mixture was stirred at room temperature for 20 min, and then a solution of FmocCl (568 mg, 2.20 mmol) in $CH_2Cl_2$ (5 mL) was added dropwise. After stirring for 2 h, aqueous HCl (2 N, 25 mL) was added and the organic layer was separated. After a further extraction of the aqueous layer with $CH_2Cl_2$ (25 mL) the combined organic layers were dried with $MgSO_4$, concentrated and the residue was purified by flash column chromatography ($CH_2Cl_2$/methanol, gradient 99:1 → 97:3), furnishing 586 mg (64%) of Fmoc-Aac as a colorless solid.

IR (neat) 3319 (NH), 3066, 2912, 2860 (CH), 1728, 1714, 1666 $cm^{-1}$ (C=O); $^1H$ NMR ($CD_3OD$, 600 MHz) $\delta$ 1.60–1.64 (m, 2H, adamantane), 1.74–1.78 (m, 6H, adamantane), 2.03–2.11 (m, 4H, adamantane), 2.53 (br s, 2H, adamantane), 4.21 (br t, 1H, $J$ = 6.7 Hz, fluorene CH), 4.31 (bd, 1H, $J$ = 6.7 Hz, $OCH_2$), 7.29 (ddd, 2H, $J$ = 7.5, 7.5, 1.1 Hz, aryl CH), 7.37 (ddd, 2H, $J$ = 7.5, 7.5, 1.2 Hz, aryl CH), 7.66 (bd, 2H, $J$ = 7.5 Hz, aryl CH), 7.78 (bd, 2H, $J$ = 7.5 Hz, aryl CH); $^{13}C$ NMR ($CDCl_3$, 150 MHz) $\delta$ 26.5, 26.7, 29.7, 32.5, 33.8, 37.5, 47.3 (6× adamantane C, fluorene CH), 63.7, 67.0 (adamantane

C, $OCH_2$), 120.0, 125.0, 127.1, 127.8, 141.4, 143.7 (6× aryl C), 155.9 (carbamate C=O).

To a suspension of commercially available Wang functionalized PS resin (100 mg, 0.11 mmol) in THF (0.5 mL) was added a solution of Fmoc-Aac (138 mg, 0.330 mmol) and $PPh_3$ (86.6 mg, 0.330 mmol) in THF (2 mL). After addition of a solution of di-*tert*-butylazodicarboxylate (76.0 mg, 0.330 mmol) in THF (approx. 1 mL), the resin was gently agitated under nitrogen for 14 h. Subsequently, the resin was separated and washed thoroughly with THF (2×), DMF (2×), methanol (2×), and $CH_2Cl_2$ (4×). Subsequently capping employing acetic acid anhydride (32 μL, 10 equiv), 2,6-collidine (45 μL, 10 equiv) and DMAP (0.4 mg, 0.1 equiv) in DMF was performed (microwave irradiation: 5 × 10 s, 50 W). After cleavage of the Fmoc protecting group, a double coupling of Fmoc-Ile-OH (134 mg, 5 equiv) using HATU (144 mg, 5 equiv) and DIPEA (130 μL, 10 equiv) in DMF (least volume possible) was carried out. The peptide was then elongated as described above. Purification (Zorbax 300SB-C18, 21.2 × 250 mm, 7 μm particles, flow: 21.2 mL/min) gradient: 5–28% A in 32 min, then isocratic elution, $t_R$: 30.1 min, ESI-MS: $[M+H]^+$; Calcd: 881.5, found: 881.5. Purity: S1: 99% ($t_R$: 18.2 min); S2: 99% ($t_R$: 18.6 min).

#### 5.5.6. Synthesis of the formally 2–3/4–5 and 2–3/4–5/6–7 shuffled NT derivatives

The respective amino acids were introduced as the following derivatives via the acylation/deprotection protocol described above: Fmoc-Ala-OH, Fmoc-Lys(Boc)-OH, Fmoc-Asn(Trt)-OH, Fmoc-Glu(OtBu)-OH, and p-Glu-OH ((*S*)2-pyrrolidone-5-carboxylic acid), in case of a positive ninhydrine test (except for proline) peptide coupling was repeated.

#### 5.5.7. pGlu-Tyr-Leu-Asn-Glu-Lys-Pro-Arg-Arg-Pro-Tyr-Ile-Leu-OH (2<->3/4<->5NT)

Purification (Zorbax Eclipse XDB-C8, 21.2 × 150 mm, 5 μm particles, eluent: 0.1% $HCO_2H$ in acetonitrile (A) and 0.1% $HCO_2H$ in $H_2O$ (B) applying a linear gradient 5–17% A in 95–83% B in 15 min, then isocratic elution, flow rate: 10 mL/min): $t_R$: 19.0 min, ESI-MS: $[M+H]^+$; Calcd: 1672.9, found: 1673.2. Purity (column/flow rate see above): System 1 (10–55% $CH_3OH$ in $H_2O$ + 0.1% $HCO_2H$ in 18 min): >99% ($t_R$: 16.5 min); System 2 (3–55% $CH_3CN$ in $H_2O$ + 0.1% $HCO_2H$ in 26 min): 99% ($t_R$: 14.2 min).

#### 5.5.8. pGlu-Tyr-Leu-Asn-Glu-Pro-Lys-Arg-Arg-Pro-Tyr-Ile-Leu-OH (2<->3/4<->5/6<->7NT)

Purification (Zorbax Eclipse XDB-C8, 21.2 × 150 mm, 5 μm particles, eluent: 0.1% $HCO_2H$ in acetonitrile (A) and 0.1% $HCO_2H$ in $H_2O$ (B) applying a linear gradient 5–18% A in 95–82% B in 18 min, then isocratic elution, flow rate: 10 mL/min): $t_R$: 19.8 min, ESI-MS: $[M+H]^+$; Calcd: 1672.9, found: 1673.2. Purity (column/flow rate see above): System 1 (10–55% $CH_3OH$ in $H_2O$ + 0.1% $HCO_2H$ in 18 min): >99% ($t_R$: 16.3 min); System 2 (3–55% $CH_3CN$ in $H_2O$ + 0.1% $HCO_2H$ in 26 min): >99% ($t_R$: 14.1 min).

### 5.6. Alignment

The alignment process followed a procedure successfully applied in homology modeling of the D2 dopamine receptor family.[15] The amino acid sequence of hNTR1 and bovine rhodopsin were retrieved from the SWISS-PROT/TrEMBL database (http://www.expasy.org).[46] Structurally conserved regions (SCRs) forming the transmembrane helices (TMs) were identified after 409 aligned sequences of members of family A GPCRs (obtained from http://www.gpcr.org/7tm) were added to the alignment.[16]

### 5.7. Construction of the homology model

The initial homology modeling process was conducted according to a protocol successfully used for the D2 dopamine receptor family,[15] based on the crystal structure of bovine rhodopsin (PDB entry 1F88)[13] and applying the SYBYL6.9 programm package (Tripos Inc., St. Louis, Missouri). Construction of the protein loops was additionally influenced by a secondary structure consensus prediction.[47] Extracellular loop (EL) 2 was modeled in analogy to bovine rhodopsin, keeping the conserved disulfide bond between Cys141 (TM3) and Cys224 (EL2) and the hairpin structure. Secondary structure consensus prediction did not indicate a preferred folding of this loop.

### 5.8. Membrane environment

The DPPC lipids were described using a previously developed topology file (Tieleman, see http://moose.bio.ucalgary.ca) and an equilibrated membrane patch consisting of 128 DPPC molecules.[18] An initial membrane, consisting of 180 DPPC molecules, was equilibrated with the GROMACS program package[23,24] under periodic boundary conditions, applying the GROMACS force field. A 0.9 nm cutoff was applied to both van der Waals and Coulomb interactions, which were completed using the particle-mesh Ewald summation.[48] Berendsen temperature bath coupling of 0.1 ps at 300 K and anisotropic pressure coupling at 1 bar in *x*, y, and *z* directions with a coupling constant of 1.0 ps were applied. All bonds were constrained by the LINCS algorithm.[49] This simulation setup was used to equilibrate the membrane template over a total simulation time of 3 ns.

Integration of the hNTR1 model into the membrane was accomplished by aligning the receptor within the membrane and removing all lipid and solvent molecules closer than 0.07 nm to the receptor with the VMD programm package.[50] Its position along the z-axis, being perpendicular to the membrane, was adjusted according to investigations by Baldwin et al.[19] The size of the simulation box was increased along the *z*-axis and water was added to the empty space. Chloride and sodium ions were added to neutralize the charge of the receptor and to create an isotonic environment (0.3 osmol).

### 5.9. Molecular dynamics simulation

After energy minimization, water and membrane were equilibrated over 1 ns of simulation time. Strong positional restraints of 1000 kJ $mol^{-1}$ $nm^{-2}$ on all atoms of the protein ensured that no artificial distortions were introduced during this process. The parameters used were the same as described above for the pure membrane patch. After this step, MD simulation continued without restraints upon the protein, until equilibrium was reached, detected by stable root mean square deviation and stable kinetic and potential energy.

A coordinate averaged receptor structure of the timeframe between 5500 and 6500 ps was calculated. In order to relax conformational strain caused by the averaging process, the resulting structure was subjected to energy minimization.

### 5.10. Docking

A docking position between the extracellular ends of TM6, TM7, and EL2 was defined for the C-terminal carboxyl function and the adjacent $C_\alpha$ and $C_\beta$ atoms of NT(8–13), allowing the carboxyl group to interact with Arg322. Mutagenesis data was introduced by means of distance restraints between ligand and receptor, taking special advantage of a correlation between receptor mutants and ligand derivatives which allowed mapping of mutant effects to

specific residues of NT(8–13).[10] Experimental data available on NT(8–13) backbone conformation by means of solid state NMR spectroscopy[6] was introduced by means of dihedral angle restraints and the construction of a ligand template backbone structure, omitting side chain atoms, except for Pro10. The MODELLER7v7 program package[22] was used to construct 100 models, applying our averaged receptor model, the ligand template structure and described restraints. Models were scored by DrugScore$^{ONLINE}$ (http://www.ag-klebe.de), applying the empirically derived scoring function DrugScore$^{CSD}$.[25] The model yielding the best score was used as a new template in an iterative docking process.

After minimization in vacuum, the final model was reintroduced into the membrane simulation box. During the first 250 ps of MD simulation only phospholipids and water molecules were allowed to move, while the receptor was fixed by strong positional restraints (1000 kJ mol$^{-1}$ nm$^{-2}$). After removing water seeping into the cleft between membrane and receptor, the simulation continued for another 250 ps. Now only the backbone was kept fixed while the side chains were allowed to move freely. Subsequently, the restraints were reduced to 100 kJ mol$^{-1}$ nm$^{-2}$ and 10 kJ mol$^{-1}$ nm$^{-2}$ over 250 ps, each. After this initial equilibration of 1 ns, restraintless MD simulation continued for another 4 ns.

### 5.11. Conformational energy maps

Conformational energy calculations were performed on the N-methylated and unmethylated tripeptide *N*-Ac-Ala-Xxx-Ala-*N*Me where Xxx = Ala and (*N*Me)Ala, applying a modified method published by Vogen et al.,[51] applying the GRIDSEARCH procedure of the Sybyl software package (Tripos Inc., St. Louis, Missouri). Sampling of *N*-Ac-Pro-Xxx-Ala-*N*Me where Xxx = Tyr and (*N*Me)Tyr was also conducted. Each map contained 5184 data points.

## Acknowledgments

We thank C.-M. Becker, Carmen Villmann and Jana Oertel (Institute of Biochemistry, FAU), Frank Boeckler (MRC, Cambridge), Harald Hübner, and Holger Bittermann for technology transfer and helpful discussions. We also acknowledge the use of the GPCR data base and the UMR cDNA Resource Center (http://www.cdna.org). This work was supported by the Deutsche Forschungsgemeinschaft (DFG Gm13/7).

## Supplementary data

Supplementary data associated with this article can be found, in the online version, at doi:10.1016/j.bmc.2008.08.051.

## References and notes

1. Boules, M.; Fredrickson, P.; Richelson, E. *Peptides* **2006**, *27*, 2523.
2. Dobner, P. R. *CMLS* **2005**, *62*, 1946.
3. Wustrow, D. J.; Davis, M. D.; Akunne, H. C.; Corbin, A. E.; Wiley, J. N.; Wise, L. D.; Heffner, T. G. *Bioorg. Med. Chem. Lett.* **1995**, *5*, 997.
4. Hadden, M. K.; Orwig, K. S.; Kokko, K. P.; Mazella, J.; Dix, T. A. *Neuropharmacology* **2005**, *49*, 1149.
5. St-Pierre, S.; Lalonde, J.-M.; Gendreau, M.; Quirion, R.; Regoli, D.; Riouxle, F. *J. Med. Chem.* **1981**, *24*, 370.
6. Luca, S.; White, J. F.; Sohal, A. K.; Filippov, D. V.; van Broom, J. H.; Grisshammer, R.; Baldus, M. *PNAS* **2003**, *100*, 10706.
7. Bittermann, H.; Einsiedel, J.; Hübner, H.; Gmeiner, P. *J. Med. Chem.* **2004**, *47*, 5587.
8. Bittermann, H.; Böckler, F.; Einsiedel, J.; Gmeiner, P. *Chem. Eur. J.* **2006**, *12*, 6315.
9. Hoffmann, T.; Lanig, H.; Waibel, R.; Gmeiner, P. *Angew. Chem., Int. Ed.* **2001**, *40*, 3361.
10. Barroso, S.; Richard, F.; Nicolas-Ethève, D.; Reversat, J.-L.; Bernassau, J.-M.; Kitabgi, P.; Labbé-Jullié, C. *J. Biol. Chem.* **2000**, *275*, 328.
11. Pang, Y.-P.; Cusack, B.; Groshan, K.; Richelson, E. *J. Biol. Chem.* **1996**, *271*, 15060.
12. Einsiedel, J.; Hübner, H.; Hervet, M.; Härterich, S.; Koschatzky, S.; Gmeiner, P. *Bioorg. Med. Chem. Lett.* **2008**, *18*, 2013.
13. Palczewski, K.; Kumasaka, T.; Hori, T.; Behnke, C. A.; Motoshima, H.; Fox, B. A.; Trong, I. L.; Teller, D. C.; Okada, T.; Stenkamp, R. E.; Yamamoto, M.; Miyano, M. *Science* **2000**, *289*, 739.
14. Oliveira, L.; Hulsen, T.; Lutje Hulsik, D.; Paiva, A. C. M.; Vriend, G. *FEBS Lett.* **2004**, *564*, 269.
15. Boeckler, F.; Lanig, H.; Gmeiner, P. *J. Med. Chem.* **2005**, *48*, 694.
16. Oliveira, L.; Paiva, A. C. M.; Vriend, G. *J. Comput. Aided Mol. Des.* **1993**, *7*, 649.
17. Seelig, A.; Seelig, J. *Biochemistry* **1974**, *13*, 4839.
18. Tieleman, D. P.; Berendsen, H. J. C. *J. Chem. Phys.* **1996**, *105*, 4871.
19. Baldwin, J. M.; Schertler, G. F. X.; Unger, V. M. *J. Mol. Biol.* **1997**, *272*, 144.
20. Hawtin, S. R.; Simms, J.; Conner, M.; Lawson, Z.; Parslow, R. A.; Trim, J.; Sheppard, A.; Wheatley, M. *J. Biol. Chem.* **2006**, *281*, 38478.
21. Williamson, P. T. F.; Bains, S.; Chung, C.; Cooke, R.; Watts, A. *FEBS Lett.* **2002**, *518*, 111.
22. Šali, A.; Blundell, T. L. *J. Mol. Biol.* **1993**, *234*, 779.
23. Berendsen, H. J. C.; van der Spoel, D.; van Drunen, R. *Comput. Phys. Commun.* **1995**, *91*, 43.
24. Lindahl, E.; Hess, B.; van der Spoel, D. *J. Mol. Model.* **2001**, *7*, 306.
25. Velec, H. F. G.; Gohlke, H.; Klebe, G. *J. Med. Chem.* **2005**, *48*, 6296.
26. MacArthur, M. W.; Thornton, J. M. *J. Mol. Biol.* **1991**, *218*, 379.
27. Cherezov, V.; Rosenbaum, D. M.; Hanson, M. A.; Rasmussen, S. G. F.; Thian, F. S.; Kobilka, T. S.; Choi, H.-J.; Kuhn, P.; Weis, W. I.; Kobilka, B. K.; Stevens, R. C. *Science* **2007**, *318*, 1258.
28. Fowler, C. B.; Pogozheva, I. D.; LeVine, H., III; Mosberg, H. I. *Biochemistry* **2004**, *43*, 8700.
29. Labbé-Jullié, C.; Barroso, S.; Nicolas-Etève, D.; Reversat, J.-L.; Botto, J.-M.; Mazella, J.; Bernassau, J.-M.; Kitabgi, P. *J. Biol. Chem.* **1998**, *273*, 16351.
30. Lawson, Z.; Wheatley, M. *Biochem. Soc. Trans.* **2004**, *32*, 1048.
31. Mehler, E. L.; Periole, X.; Hassan, S. A.; Weinstein, H. *J. Comput. Aided Mol. Des.* **2002**, *16*, 841.
32. Sherman, W.; Day, T.; Jacobson, M. P.; Friesner, R. A.; Farid, R. *J. Med. Chem.* **2006**, *49*, 534.
33. Monné, M.; Nilsson, I.; Johansson, M.; Elmhed, N.; von Heijne, G. *J. Mol. Biol.* **1998**, *284*, 1177.
34. Richard, F.; Barroso, S.; Nicolas-Ethève, D.; Kitabgi, P.; Labbé-Jullié, C. *Eur. J. Pharmacol.* **2001**, *433*, 63.
35. Klco, J. M.; Nikiforovich, G. V.; Baranski, T. J. *J. Biol. Chem.* **2006**, *281*, 12010.
36. González-Muñiz, R.; García-López, M. T.; Gómez-Monterrey, I.; Herranz, R.; Jimeno, M. L.; Suárez-Gea, M. L.; Johansen, N. L.; Thøgersen, H.; Suzdak, P. *J. Med. Chem.* **1995**, *38*, 1015.
37. Archer, E.; Maigret, B.; Escrieut, C.; Pradayrol, L.; Fourmy, D. *TiPS* **2003**, *24*, 36.
38. Antonelli, T.; Fuxe, K.; Tomasisni, M. C.; Mazzoni, E.; Agnati, L. F.; Tanganelli, S.; Ferraro, L. *Prog. Neurobiol.* **2007**, *83*, 92.
39. Breitinger, H. C.; Villmann, C.; Becker, K.; Becker, C.-M. *J. Biol. Chem.* **2001**, *276*, 29657.
40. Graham, F. L.; van der Eb, A. J. *Virology* **1973**, *52*, 456.
41. Lowry, O. H.; Rosebrough, N. J.; Farr, A. L.; Randall, R. J. *J. Biol. Chem.* **1951**, *193*, 265.
42. Cheng, Y. C.; Prusoff, W. H. *Biochem. Pharmacol.* **1973**, *22*, 3099.
43. Lee, S. P.; So, C. H.; Rashid, A. J.; Varghese, G.; Cheng, R.; Lança, A. J.; O'Dowd, B. F.; George, S. R. *J. Biol. Chem.* **2004**, *279*, 35671.
44. Kassack, M. U.; Höfgen, B.; Lehmann, J.; Eckstein, N.; Quillan, J. M.; Sadee, W. *J. Biomol. Screening* **2002**, *7*, 233.
45. Falb, E.; Yechezkel, T.; Salitra, Y.; Gilon, C. *J. Pept. Res.* **1999**, *53*, 507.
46. O'Donovan, C.; Martin, M. J.; Gattiker, A.; Gasteiger, E.; Bairoch, A.; Apweiler, R. *Brief. Bioinform.* **2002**, *3*, 275.
47. Combet, C.; Blanchet, C.; Geourjon, C.; Deléage, G. *TIBS* **2000**, *25*, 147.
48. Darden, T.; York, D.; Pederson, L. *J. Chem. Phys.* **1993**, *98*, 10089.
49. Hess, B.; Bekker, H.; Berendsen, H. J. C.; Fraaije, J. G. E. M. *J. Comput. Chem.* **1997**, *18*, 1463.
50. Humphrey, W.; Dalke, A.; Schulten, K. *J. Mol. Graphics Modell.* **1996**, *14*, 33.
51. Vogen, S. M.; Paczkowski, N. J.; Kirnasky, L.; Short, A.; Whitmore, J. B.; Sherman, S. A.; Taylor, S. M.; Sanderson, S. D. *Int. Immunopharmacol.* **2001**, *1*, 2151.